nature nanotechnology

ARTICLES

https://doi.org/10.1038/s41565-020-0730-5

Imaging strain-localized excitons in nanoscale bubbles of monolayer WSe_2 at room temperature

Thomas P. Darlington[1], Christian Carmesin[2], Matthias Florian[2], Emanuil Yanev[3], Obafunso Ajayi[3], Jenny Ardelean[3], Daniel A. Rhodes[3], Augusto Ghiotto[4], Andrey Krayev[5], Kenji Watanabe[6], Takashi Taniguchi[6], Jeffrey W. Kysar[3], Abhay N. Pasupathy[4], James C. Hone[3], Frank Jahnke[2]✉, Nicholas J. Borys[7]✉ and P. James Schuck[3]✉

In monolayer transition-metal dichalcogenides, localized strain can be used to design nanoarrays of single photon sources. Despite strong empirical correlation, the nanoscale interplay between excitons and local crystalline structure that gives rise to these quantum emitters is poorly understood. Here, we combine room-temperature nano-optical imaging and spectroscopic analysis of excitons in nanobubbles of monolayer WSe_2 with atomistic models to study how strain induces nanoscale confinement potentials and localized exciton states. The imaging of nanobubbles in monolayers with low defect concentrations reveals localized excitons on length scales of around 10 nm at multiple sites around the periphery of individual nanobubbles, in stark contrast to predictions of continuum models of strain. These results agree with theoretical confinement potentials atomistically derived from the measured topographies of nanobubbles. Our results provide experimental and theoretical insights into strain-induced exciton localization on length scales commensurate with exciton size, realizing key nanoscale structure–property information on quantum emitters in monolayer WSe_2.

The intense light–matter interactions of two-dimensional (2D) monolayer transition-metal dichalcogenides (1L-TMDs) are mediated by a diverse suite of excitonic phenomena[1–3] that present a wealth of opportunities for novel optoelectronic functionalities in areas spanning from high-performance sensing and non-traditional photovoltaics to the quantum information sciences. Many of these opportunities emerge from—and heavily rely on—the unique ways in which the 2D transition-metal dichalcogenide (TMD) semiconductors enable the manipulation of excitonic phenomena on the nanoscale. Within this collection of capabilities[4–8], strain engineering is pre-eminent, offering unprecedented flexibility and precision, and opening new routes to highly tailored optoelectronic materials. Extrinsic strains of up to several per cent can be endured without fracture[9–11] and have been shown to continuously reduce the optical bandgap[9,12] as well as to modify the exciton–phonon coupling, thus narrowing the photoluminescence linewidth[13]. Further, such strain can be localized, embedding nanoscale potential energy wells for the funnelling and localization of excitons[14–16]. Notably, in 1L-WSe_2, it has become evident that local strain is a key ingredient for the formation of low-temperature quantum emitters[11,17,18] and that strain engineering can potentially extend their operating range to room temperature[19,20]. The resulting highly integrable solid-state non-classical light sources[21] underscore the technological potential of harnessing strain to engineer nanoscale exciton localization in 2D TMD semiconductors.

Despite the observations of exciton funnelling and single-photon emission in localized strained regions of 2D TMDs, an understanding of the induced exciton localization is notably lacking, especially on the nanoscale. This absence of a fundamental picture has led to critical ambiguities, particularly concerning the formation of quantum emitters in 1L-WSe_2, in which the roles and interplay between strain, excitons and crystallographic defects remain largely a mystery. For instance, it has been shown that the quantum emission can be co-localized with a nanobubble[11], where strain models derived from continuum elastic plate theory predict that a single region of maximum strain (and thus exciton localization) occurs at the apex of the nanobubble[9,10]. However, multiple emitters per nanobubble are typically observed[18,22–25], which is at odds with a single localization site and suggests a possible role of crystallographic defect states or some other sub-nanobubble inhomogeneity[11]. Recently, improved microscopic theoretical models have predicted that quantum dot-like electronic states in TMDs can form within nanobubbles in the absence of defects[26,27]. In particular, a first-principles approach that carefully considers the strain-induced atomic structure[27] (and which we employ here) has predicted that strain maxima and multiple low-energy states form in a doughnut-like distribution near the nanobubble periphery. This surprising strain distribution is an apparent result of atomic-scale wrinkling around the edges of highly strained nanobubbles, leading to more localized lower-energy states relative to the case of a nanobubble with a smooth topography. Such predicted states provide the critical missing piece of the puzzle for understanding and controlling the strain localization of excitons in 2D TMD semiconductors. However, due to their nanoscale size and distribution within a nanobubble, these localized energy states cannot be directly resolved with far-field optical characterization methods, necessitating interrogation by more sophisticated higher-resolution techniques.

In this work, we employed apertureless scanning near-field optical microscopy to image the localized exciton (LX) states within nanobubbles of 1L-WSe_2. Using hyperspectral nanophotoluminescence

[1]Department of Physics, UC Berkeley, Berkeley, CA, USA. [2]Institute for Theoretical Physics, University of Bremen, Bremen, Germany. [3]Department of Mechanical Engineering, Columbia University, New York, NY, USA. [4]Department of Physics, Columbia University, New York, NY, USA. [5]Horiba Scientific, Novato, CA, USA. [6]National Institute for Materials Science, Tsukuba, Japan. [7]Department of Physics, Montana State University, Bozeman, MT, USA. ✉e-mail: jahnke@itp.uni-bremen.de; nicholoas.borys@montana.edu; p.j.schuck@columbia.edu

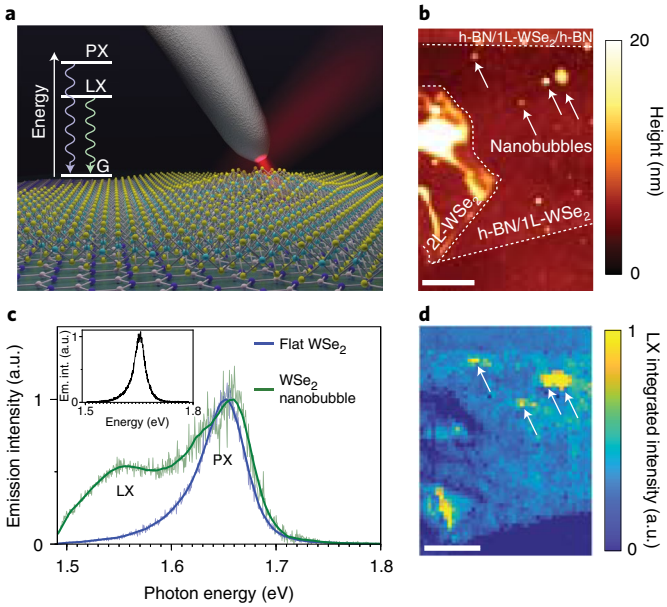

Fig. 1 | Nano-optical detection of room-temperature photoluminescence from LX states in nanobubbles in 1L-WSe_2. a, Schematic of the room-temperature nanophotoluminescence imaging and spectroscopic analysis of 1L-WSe_2 on top of h-BN (not to scale). Inset: simple energy-level diagram illustrating the energetic ordering of the primary exciton (PX), localized exciton (LX) and ground (G) states of 1L-WSe_2. **b**, AFM topography image of the exfoliated 1L-WSe_2 flake on top of the h-BN substrate. The white arrows indicate several nanobubbles in the 1L-WSe_2. 2L, bilayer. **c**, Comparison of the nanophotoluminescence emission spectra collected from a flat region and a nanobubble in the 1L-WSe_2 with a resolution of 30 nm. Inset: typical far-field spectrum of the 1L-WSe_2. **d**, Spatial map of the intensity of LX emission (integration intensity range 1.5–1.6 eV) showing that the LX states in 1L-WSe_2 are localized in spatially discrete regions that correspond to nanobubbles in the topography. All scale bars, 500 nm. For the nano-optical data, the integration time per pixel is 150 ms, and the pixel size is $20 \times 20\ nm^2$.

mapping, we achieved a sub-34 nm spatial resolution and resolved individual localized low-energy states that are separated by distances of less than 50 nm within single nanobubbles at room temperature. Furthermore, we observed that these localized states form in doughnut-like patterns, which is consistent with the first-principles predictions[27] that refine those of continuum plate and membrane models[9,10]. These LXs are also identified in nanobubbles of 'flux-grown' 1L-WSe_2, which has a much lower defect density as compared with monolayers exfoliated from commercially available crystals (~100-fold lower defect density)[28]. Our results are consistent and reproducible across multiple samples and numerous bubbles ($N > 50$; see, for example, Supplementary Fig. 1). The combination of nano-optical characterization with atomistic modelling and materials engineering indicates that (1) exciton localization by inhomogeneous strain occurs through the formation of wrinkles near the edges and bending near the base of nanobubbles, (2) these excitons remain localized at elevated (room) temperature and (3) the optical emission of LXs at room temperature can be enhanced by nano-optical/plasmonic techniques by at least 100-fold. Together, these findings provide key experimental evidence for highly confined localized states in nanobubbles, which constitutes a new paradigm of nanoscale strain engineering in 2D TMD semiconductors that is particularly relevant for developing non-classical light sources for practical quantum optical devices.

Nano-optics of nanobubbles of WSe_2

Numerous processes that are critical for developing advanced functionalities and devices with 1L-TMD semiconductors have been studied with nano-optical methods, revealing a rich suite of highly localized optoelectronic phenomena[29–33]. Figure 1a illustrates the experimental configuration of our nanophotoluminescence investigations of individual nanobubbles of 1L-WSe_2 in which a sharp silver tip (Horiba) has been positioned within 2 nm of the 1L-WSe_2 (Fig. 1a). A complete discussion of the experimental techniques is presented in the Supplementary Information. Briefly, the tip–sample junction was illuminated from the side with *p*-polarized, continuous-wave laser excitation (637.27 nm, 75–100 μW) at an oblique angle of incidence such that the induced polarization of the tip can couple with the in-plane and out-of-plane transition dipoles[34,35]. As the sample was raster-scanned, nanophotoluminescence from the tip–sample junction and the local topography of the 1L-WSe_2 were simultaneously recorded.

As indicated in the atomic force microscopy (AFM) micrograph (Fig. 1b), the entirety of the 1L-WSe_2 in Figs. 1–3 is supported by an underlying crystal of hexagonal boron nitride (h-BN; ~200-nm thick), forming a 2D 1L-WSe_2/h-BN heterostructure. We note that a portion of this 1L-WSe_2 flake is fully encapsulated and covered by a second, thin h-BN crystal (~3 nm). However, all of the results presented here were acquired from the exposed 1L-WSe_2 that is directly accessible to the nano-optical antenna (as illustrated in Fig. 1a). Details of the 'dry-stamping' sample fabrication process are provided in an earlier report[11] and the Supplementary Information. This process is known to produce structural 'imperfections' such as nanobubbles, tears, folds and wrinkles. In our case, a portion of the 1L-WSe_2 folded on top of itself to form a bilayer and several pronounced creases (Fig. 1b). In addition, small topographical nanobubbles, with characteristic heights of ~2–10 nm, are observed in the 1L-WSe_2 and are attributed to trapped substances between the layers[10]. Such nanobubbles have been repeatedly observed in heterostructures of layered materials[11,15,36], and as noted above, correlate with quantum emitters in 1L-WSe_2 at cryogenic temperatures[11].

Figure 1c contrasts the nanophotoluminescence spectra collected from a flat region and a nanobubble of the 1L-WSe_2 at room temperature. The spectrum of the flat region is composed of the standard excitonic photoluminescence of 1L-WSe_2 at ~1.65 eV[29,37], which we will refer to as the primary exciton (PX). The emission spectrum recorded when the nano-optical antenna was positioned over a nanobubble is dramatically different, exhibiting redshifted excitonic emission and an additional intense low-energy emission band centred at ~1.56 eV, as determined by Gaussian peak fitting (Supplementary Fig. 2 and Supplementary Methods). We note in these spectra that there is increased noise in the region of the PX state due to the subtraction of the far-field signal, as discussed in the Supplementary Information. In the 1L-WSe_2, every region that was found to exhibit strong low-energy emission correlated with a nanobubble (see white arrows in Figs. 1b and 1d). A selection of such emission spectra from four individual nanobubbles together with their associated topographies is shown in Supplementary Fig. 3. The lateral extents of the nanobubbles are in the range of ~30–140 nm with heights of 1.5–20 nm and, depending on size, they exhibit a diverse set of broad emission spectra, some of which show signatures of multiple low-energy states. In general, low-energy emission occurs at emission energies that span a range of about 70 meV (from ~80 to ~150 meV below the PX) and exhibits linewidths of ~150 meV that are attributed to thermal broadening[20] and plasmonic coupling to the tip[38].

Close inspection of the nanophotoluminescence spectra in Fig. 1c reveals several characteristics of the low-energy photoluminescence that are different from the well-studied PX state. First, we concurrently observe both the low-energy emission and strong emission at ~1.65 eV, corresponding to the PX spectra measured in

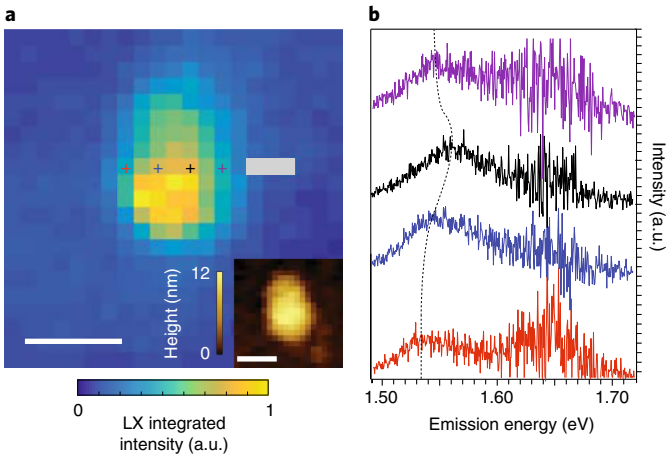

Fig. 2 | High-resolution nanophotoluminescence imaging and spectroscopy of distinct LX states within a single nanobubble. a, Nanophotoluminescence image of the spatial distribution of LX emission (integrated intensity range 1.5–1.6 eV) of a single nanobubble. The three white pixels are a scanning artefact where the nano-optical signal was not acquired. Scale bar, 100 nm. Inset: AFM topography image of the nanobubble. Scale bar, 100 nm. Its overall height is 12 nm and its average radius is 74 nm. **b,** Sample emission spectra from the corresponding points marked with crosses in panel **a**. The distance between the red and blue marks is 45 nm. For the nano-optical data, the integration time per pixel is 100 ms, and the pixel size is 17 × 17 nm^2.

the far field (inset in Fig. 1c), within our nano-optical mode volume. Second, the low-energy band here is well below the energies of other native excitonic complexes in this material (for example, trions, the dark exciton[39,40] and biexcitons[41]) and in an energetic region that is often associated with defect states[41]. Third, the linewidth is substantially larger than that of the PX, which contrasts with what has been observed for strain-tuned PX states[13]. Finally, the energy separation of this band with respect to the PX state (see also Supplementary Fig. 2) and its localization in nanobubble regions are in line with the corresponding observations for single-photon emitter states at cryogenic temperatures in bare 1L-WSe_2 (refs. [11,18]) and 1L-WSe_2 coupled to a plasmonic cavity[20,42,43]. Based on these considerations, we deduce that this low-energy band, which is amplified by the nano-optical antenna (consistent with the observation in ref. [20] of plasmon-enhanced localized emission at elevated temperatures), originates from LX states in the nanobubbles.

Nanophotoluminescence directly probes the LX emission on length scales that are commensurate with—or even smaller than—the nanobubbles themselves, allowing us to explore the origins of the diverse emission spectra and nanoscale structure–property relationships in more detail. Here, we estimated that our spatial resolution is ~34 nm (see Supplementary Fig. 4 and the associated discussion of our resolution estimate). In Fig. 2, the spatial distribution of the LX emission is shown for a larger nanobubble (radius of ~75 nm, peak height of 12 nm, aspect ratio of 0.16). From the nanophotoluminescence, we resolved nanoscale variations in the LX emission within the nanobubble itself (Fig. 2a), finding that the integrated emission intensity is not uniform. Rather, it is concentrated in specific locations of the nanobubble that do not correspond to its apex (cf. inset of Fig. 2a). Furthermore, different points of the nanobubble that are separated by distances as small as 30 nm clearly exhibit distinct spectra (Fig. 2b). The dashed line linking the maxima of the LX spectral peaks clearly shows that the lower-energy LX states are positioned at the edges of the nanobubble, where the maximum confinement potential and the formation of wrinkles are expected to occur. The systematic localization of lower-energy emitters at the edges of the nanobubble is further confirmed by a comparison of the average emission spectrum of the nanobubble periphery with that of the centre, as presented in Supplementary Figs. 5 and 6. Clearly, larger nanobubbles host multiple emissive localization centres for LXs, an effect that to date has only been inferred spectroscopically[11,43].

Theoretical analysis of exciton confinement in nanobubbles

Our hyperspectral mapping of the nanobubble in Fig. 2 shows that the lowest-energy states (and thus the deepest confinement potentials) are concentrated around the edge. To gain more insight into the physical mechanism, we applied the theory set out in ref. [27], which considers the influence of local strain within the nanobubbles on the local electronic and optical properties. Our method is based on atomistic calculations in which the relevant part of the nanostructure is modelled using a lattice of atomic sites. For the calculations, we used the nanobubble geometry obtained from the AFM measurements and determined the corresponding relaxed positions of the individual atoms by a valence force field simulation. The results provide the strain field in the structure and confirm the existence of atomic-scale wrinkling. In a second step, the information on the displaced atomic positions was used within a tight-binding calculation to quantify how the strain field of the individual atoms within the nanobubble translates into confinement potentials and local electronic states.

The calculated confinement potentials (Fig. 3a) for the nanobubble topography derived from the AFM data in Fig. 2a (inset) exhibit a doughnut pattern, with deeper potentials located on the nanobubble periphery that trace the wrinkling effect (Fig. 3b) and its associated regions of large shear strain (Fig. 3c; see also all the in-plain strain components in Supplementary Fig. 7 and the accompanying discussion). The theoretical confinement potentials correspond remarkably well with the nanoscale spatial distribution of the measured LX energies (Fig. 3d; see the Supplementary Information for fitting details). This correspondence is further in direct accordance with the experimental spectra in Fig. 2b, which shows that the low-energy emission is isolated in the nanobubble periphery. To demonstrate the correlation between the theoretical predictions and experimental data, the measured LX energy was plotted against the predicted confinement potential at the corresponding region of the nanobubble (Fig. 3e; see the Supplementary Information for analysis details). Around the periphery of the nanobubble, a strong correlation between LX energy and the depth of the confinement potential is observed: regions of stronger confinement correspond to lower LX energy. In contrast, in the central region, very little correlation of energy with confinement potential is observed, which suggests a lack of strongly confined excitons in that area (masks for each of these regions are shown in Supplementary Fig. 6). This different behaviour may indicate a more general exciton funnelling effect in the central region[14], whereas the periphery is dominated by highly confined states.

Influence of defects

The correspondence between the theoretical analysis of the strain and resulting electronic states within the nanobubble and our nano-optical dataset presented in Fig. 3 strongly suggests that the experimentally observed localized states are the predicted quantum dot-like states[27]. In principle, point defects in the 1L-WSe_2 lattice can also localize excitons in a similarly inhomogeneous way. To better elucidate the potential role of defects, we repeated our nanobubble photoluminescence mapping and theoretical calculations in high-quality flux-grown 1L-WSe_2, which has been shown to have defect densities approximately two orders of magnitude lower than commercially grown crystals, providing an average spacing between defects on the order of our nano-optical resolution[28]. As shown in detail in the Supplementary Information, every nanobubble

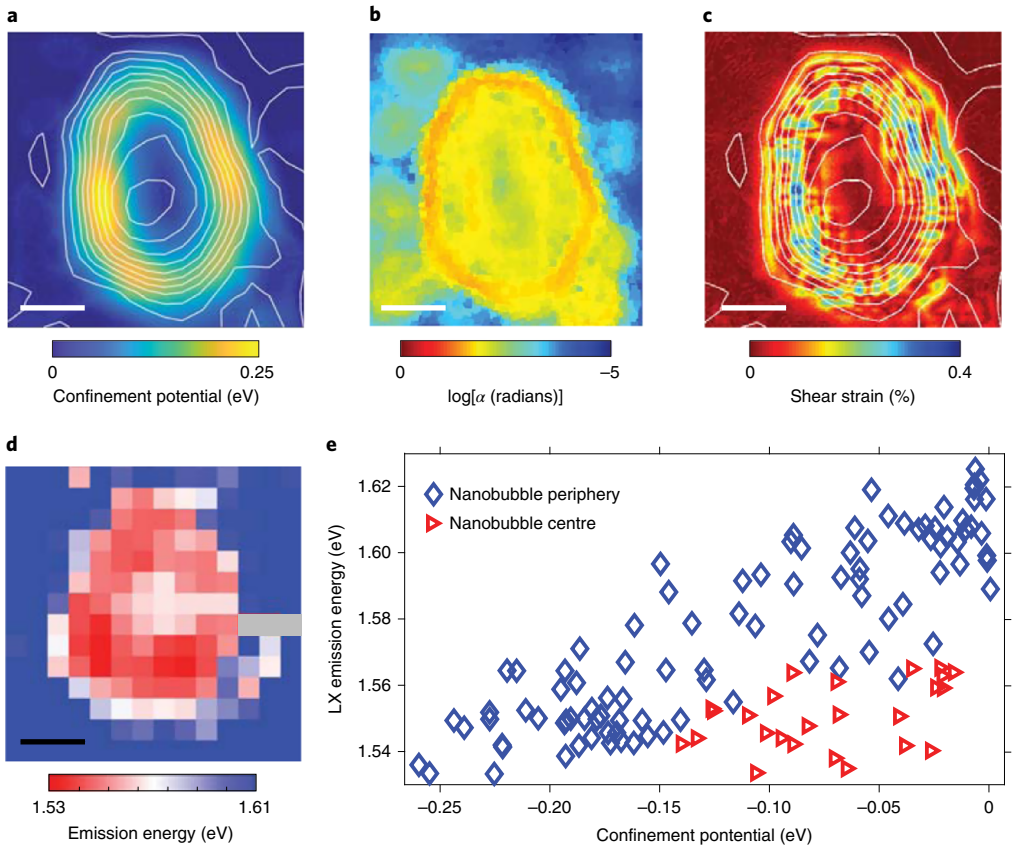

Fig. 3 | Comparison of atomistic theory with experimental data. a, Calculated carrier confinement potential for the nanobubble topography shown in the inset of Fig. 2a. The solid lines represent topographic contours based on the AFM measurement. **b**, Corresponding values of the surface normal deviation, defined as the average angle, α, between normal vectors at neighbouring unit cells, obtained from relaxed atomic positions, showing wrinkling of the lattice. **c**, Map of the shear component of the strain tensor, originating from local wrinkling of the lattice. The positive values indicate larger atomic distances leading to a local reduction of the bandgap. **d**, Spatial map of the LX emission energy of the nanophotoluminescence data shown in Fig. 2. **e**, Correlation between the local confinement potentials shown in **a** and the LX emission energies shown in **d**. The data points are separated into points at the centre of the nanobubble (red triangles) and points at the periphery of the nanobubble (blue diamonds). All scale bars, 50 nm. The theoretical calculations with atomic resolution are scaled up by a factor of five (see the Supplementary Information).

identified in this higher-quality material exhibits similar LX emission to that of the commercial material (see Supplementary Fig. 1 and the corresponding discussion). More specifically, the occurrence of the LX emission band in the nanobubbles does not depend on the defect density in the ranges probed here.

In Fig. 4, we provide a collage of four nanobubbles in the monolayer area of the high-quality (that is, flux-grown) 1L-WSe_2. Figure 4a,b shows the measured AFM topography images of the four nanobubbles and their corresponding spatial distributions of LX emission energies, respectively. Here, the nanophotoluminescence measurements were performed with optical excitation at 785 nm, which is below the energy of the PX and enhances the contrast between the LX and PX states, allowing the LX states to be observed with a greater signal-to-noise ratio (see the Supplementary Information). Figure 4c–e show the calculated confinement potentials, overlap of the electron–hole wave functions and the predicted shifts in photoluminescence emission energies, respectively. As with the nanobubble shown in Fig. 3b, each nanobubble in the flux-grown 1L-WSe_2 exhibits lower-energy emission at the nanobubble periphery. This peripheral spatial distribution of low-energy states is replicated in the predicted confinement potentials and electron–hole wave-function overlap shown in Fig. 4c,d, respectively. Finally, the predicted photoluminescence energy shifts and corresponding spatial distributions shown in Fig. 4e agree well with the measured LX emission energies presented in Fig. 4b. Considering the challenges of room-temperature hyperspectral imaging on the 10–20-nm scale, the limitation of the topographical maps in Fig. 4a to a resolution of ~15 nm, as well as the complexities of directly incorporating these measurements into a feasible atomistic model (for details, see the Supplementary Information), the agreement between experiment and theory is particularly remarkable.

The similarities between Figs. 3 and 4, despite dramatically different defect densities, suggest that the LX emission distribution in nanobubbles is not substantially determined by atomic defects in the lattice. As noted above, because there is on average approximately one defect in every 15 nm × 15 nm in flux-grown material, which is close to the spatial resolution of the nano-optical probe, major defect-associated optical changes would be resolvable. Although defects may still play a role in the emission, the implication here is that the primary effect in terms of the nanoscale spatial distribution and the creation of quantum dot-like states is the local strain profile, with localized regions of maximum strain occurring at locations around the edge of nanobubbles. However, it is certainly possible that defects play a role in, for example, the further localization or the exact distribution of wrinkles on the atomic scale. Such ångstrom-level effects are beyond the resolution of our current nano-optical probes, which use AFM tips with radii of curvature ranging from ~15 to ~40 nm. Future correlations with, for example, atomic-resolution AFM[44], atomic-resolution transmission electron microscopy or combined cathodoluminescence and electron

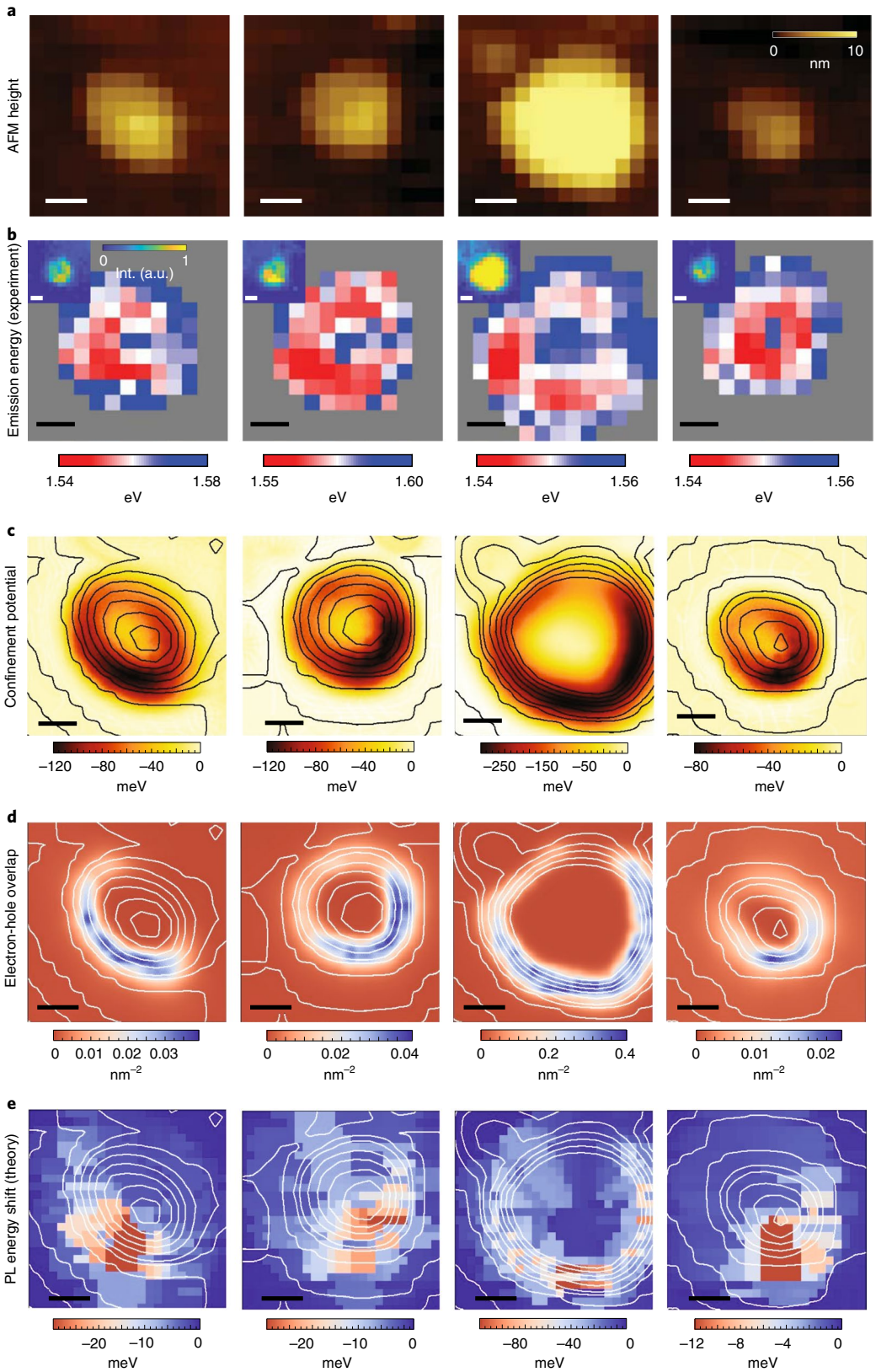

Fig. 4 | Comparison of experiment and theory for four nanobubbles in 1L-WSe_2 with a low concentration of defects. a,**b**, AFM topography images (**a**) and nanophotoluminescence emission energies (**b**) of the LX state, respectively. The images in **a** reveal the heights of the nanobubbles. The insets in **b** show the integrated nanophotoluminescence intensity after low-pass energy filtering to isolate the LX emission. **c**, Theoretical confinement potentials obtained from the displaced atomic positions derived from nanobubble strain calculations[46,47] and Harrison's rule[48]. **d**,**e**, Electron–hole wave-function overlap (**d**) and predicted photoluminescence energy shifts (**e**) of the nanobubbles, respectively. The solid lines in **c**–**e** represent the topographic contours of the AFM measurements shown in **a**. All scale bars, 50 nm. The theoretical calculations with atomic resolution are scaled up by a factor of five (see the Supplementary Information). For the nano-optical data in **b**, the integration time per pixel is 200 ms, and the pixel size is $20 \times 20\ nm^2$.

diffraction measurements, as recently demonstrated with single quantum emitters in h-BN (ref. [45]), may enable these effects to be mapped on the atomic scale, providing the ultimate picture of localized states in 2D monolayer semiconductors.

Conclusion

By using nano-optical techniques, strain-localized exciton states within single nanobubbles of 1L-WSe_2 have been observed at room temperature with localization lengths of less than 50 nm that are markedly smaller than the nanobubble itself. In general, the spatial distribution of these low-energy states forms a doughnut-like pattern around the periphery of the nanobubble, surrounding a region of higher-energy states at the centre, which is consistent with previous theoretical predictions of atomic-scale strain effects. By integrating the experimentally determined topography with this atomistic model, the experimental results are qualitatively replicated by the theoretical model, establishing the first robust experiment–theory connection for the formation of strain-induced quantum-dot states in monolayer TMD semiconductors. Furthermore, these findings were reproduced in flux-grown 1L-WSe_2 with orders-of-magnitude lower defect densities, implying that the nanoscale localization is primarily influenced by strain and not crystalline defects. Our results show that LX states accessed with nano-optical techniques remain localized at room temperature, leading to compelling potential applications in practical strain-engineered optoelectronic and quantum optical architectures.

Online content

Any methods, additional references, Nature Research reporting summaries, source data, extended data, supplementary information, acknowledgements, peer review information; details of author contributions and competing interests; and statements of data and code availability are available at https://doi.org/10.1038/s41565-020-0730-5.

Received: 13 January 2020; Accepted: 3 June 2020;
Published online: 13 July 2020

References

1. Yao, K. et al. Optically discriminating carrier-induced quasiparticle band gap and exciton energy renormalization in monolayer MoS_2. *Phys. Rev. Lett.* **119**, 087401 (2017).
2. Mak, K. F. et al. Tightly bound trions in monolayer MoS_2. *Nat. Mater.* **12**, 207–211 (2013).
3. Raja, A. et al. Coulomb engineering of the bandgap and excitons in two-dimensional materials. *Nat. Commun.* **8**, 15251 (2017).
4. Unuchek, D. et al. Room-temperature electrical control of exciton flux in a van der Waals heterostructure. *Nature* **560**, 340–344 (2018).
5. Alexeev, E. M. et al. Resonantly hybridized excitons in moiré superlattices in van der Waals heterostructures. *Nature* **567**, 81–86 (2019).
6. Jin, C. H. et al. Observation of moiré excitons in WSe_2/WS_2 heterostructure superlattices. *Nature* **567**, 76–80 (2019).
7. Seyler, K. L. et al. Signatures of moiré-trapped valley excitons in $MoSe_2/WSe_2$ heterobilayers. *Nature* **567**, 66–70 (2019).
8. Tran, K. et al. Evidence for moiré excitons in van der Waals heterostructures. *Nature* **567**, 71–75 (2019).
9. Lloyd, D. et al. Band gap engineering with ultralarge biaxial strains in suspended monolayer MoS_2. *Nano Lett.* **16**, 5836–5841 (2016).
10. Khestanova, E., Guinea, F., Fumagalli, L., Geim, A. K. & Grigorieva, I. V. Universal shape and pressure inside bubbles appearing in van der Waals heterostructures. *Nat. Commun.* **7**, 12587 (2016).
11. Shepard, G. D. et al. Nanobubble induced formation of quantum emitters in monolayer semiconductors. *2D Mater.* **4**, 021019 (2017).
12. Desai, S. B. et al. Strain-induced indirect to direct bandgap transition in multilayer WSe_2. *Nano Lett.* **14**, 4592–4597 (2014).
13. Niehues, I. et al. Strain control of exciton–phonon coupling in atomically thin semiconductors. *Nano Lett.* **18**, 1751–1757 (2018).
14. Feng, J., Qian, X., Huang, C.-W. & Li, J. Strain-engineered artificial atom as a broad-spectrum solar energy funnel. *Nat. Photonics* **6**, 866–872 (2012).
15. Tyurnina, A. V. et al. Strained bubbles in van der waals heterostructures as local emitters of photoluminescence with adjustable wavelength. *ACS Photonics* **6**, 516–524 (2019).
16. Li, H. et al. Optoelectronic crystal of artificial atoms in strain-textured molybdenum disulphide. *Nat. Commun.* **6**, 7381 (2015).
17. Branny, A., Kumar, S., Proux, R. & Gerardot, B. D. Deterministic strain-induced arrays of quantum emitters in a two-dimensional semiconductor. *Nat. Commun.* **8**, 15053 (2017).
18. Tonndorf, P. et al. Single-photon emission from localized excitons in an atomically thin semiconductor. *Optica* **2**, 347–352 (2015).
19. Rosenberger, M. R. et al. Quantum calligraphy: writing single-photon emitters in a two-dimensional materials platform. *ACS Nano* **13**, 904–912 (2019).
20. Luo, Y., Liu, N., Li, X., Hone, J. C. & Strauf, S. Single photon emission in WSe_2 up 160 K by quantum yield control. *2D Mater.* **6**, 035017 (2019).
21. Aharonovich, I., Englund, D. & Toth, M. Solid-state single-photon emitters. *Nat. Photonics* **10**, 631–641 (2016).
22. He, Y. M. et al. Single quantum emitters in monolayer semiconductors. *Nat. Nanotechnol.* **10**, 497–502 (2015).
23. Koperski, M. et al. Single photon emitters in exfoliated WSe_2 structures. *Nat. Nanotechnol.* **10**, 503–506 (2015).
24. Srivastava, A. et al. Optically active quantum dots in monolayer WSe_2. *Nat. Nanotechnol.* **10**, 491–496 (2015).
25. Chakraborty, C., Kinnischtzke, L., Goodfellow, K. M., Beams, R. & Vamivakas, A. N. Voltage-controlled quantum light from an atomically thin semiconductor. *Nat. Nanotechnol.* **10**, 507–511 (2015).
26. Chirolli, L., Prada, E., Guinea, F., Roldán, R. & San-Jose, P. Strain-induced bound states in transition-metal dichalcogenide bubbles. *2D Mater.* **6**, 025010 (2019).
27. Carmesin, C. et al. Quantum-dot-like states in molybdenum disulfide nanostructures due to the interplay of local surface wrinkling, strain, and dielectric confinement. *Nano Lett.* **19**, 3182–3186 (2019).
28. Edelberg, D. et al. Approaching the intrinsic limit in transition metal diselenides via point defect control. *Nano Lett.* **19**, 4371–4379 (2019).
29. Park, K. D. et al. Hybrid tip-enhanced nanospectroscopy and nanoimaging of monolayer WSe_2 with local strain control. *Nano Lett.* **16**, 2621–2627 (2016).
30. Lin, Z. et al. 2D materials advances: from large scale synthesis and controlled heterostructures to improved characterization techniques, defects and applications. *2D Mater.* **3**, 042001 (2016).
31. Kastl, C. et al. The important role of water in growth of monolayer transition metal dichalcogenides. *2D Mater.* **4**, 021024 (2017).
32. Bao, W. et al. Visualizing nanoscale excitonic relaxation properties of disordered edges and grain boundaries in monolayer molybdenum disulfide. *Nat. Commun.* **6**, 7993 (2015).
33. Lee, Y. et al. Near-field spectral mapping of individual exciton complexes of monolayer WS_2 correlated with local defects and charge population. *Nanoscale* **9**, 2272–2278 (2017).
34. Ogletree, D. F. et al. Near-field imaging: revealing optical properties of reduced-dimensionality materials at relevant length scales. *Adv. Mater.* **27**, 5692–5692 (2015).
35. Schuck, P. J., Bao, W. & Borys, N. J. A polarizing situation: taking an in-plane perspective for next-generation near-field studies. *Front. Phys.* **11**, 117804 (2016).
36. Haigh, S. J. et al. Cross-sectional imaging of individual layers and buried interfaces of graphene-based heterostructures and superlattices. *Nat. Mater.* **11**, 764–767 (2012).
37. Shi, W. et al. Raman and photoluminescence spectra of two-dimensional nanocrystallites of monolayer WS_2 and WSe_2. *2D Mater.* **3**, 025016 (2016).
38. Eggleston, M. S., Messer, K., Zhang, L., Yablonovitch, E. & Wu, M. C. Optical antenna enhanced spontaneous emission. *Proc. Natl Acad. Sci. USA* **112**, 1704–1709 (2015).
39. Zhang, X. X., You, Y., Zhao, S. Y. & Heinz, T. F. Experimental evidence for dark excitons in monolayer WSe_2. *Phys. Rev. Lett.* **115**, 257403 (2015).
40. Park, K. D., Jiang, T., Clark, G., Xu, X. D. & Raschke, M. B. Radiative control of dark excitons at room temperature by nano-optical antenna-tip Purcell effect. *Nat. Nanotechnol.* **13**, 59–64 (2018).
41. Chow, P. K. et al. Defect-induced photoluminescence in monolayer semiconducting transition metal dichalcogenides. *ACS Nano* **9**, 1520–1527 (2015).
42. Luo, Y. et al. Deterministic coupling of site-controlled quantum emitters in monolayer WSe_2 to plasmonic nanocavities. *Nat. Nanotechnol.* **13**, 1137–1142 (2018).
43. Kern, J. et al. Nanoscale positioning of single-photon emitters in atomically thin WSe_2. *Adv. Mater.* **28**, 7101–7105 (2016).
44. Chiang, C. L., Xu, C., Han, Z. M. & Ho, W. Real-space imaging of molecular structure and chemical bonding by single-molecule inelastic tunneling probe. *Science* **344**, 885–888 (2014).

45. Hayee, F. et al. Revealing multiple classes of stable quantum emitters in hexagonal boron nitride with correlated optical and electron microscopy. *Nat. Mater.* **19**, 534–539 (2020).
46. van Duin, A. C. T., Dasgupta, S., Lorant, F. & Goddard, W. A. ReaxFF: a reactive force field for hydrocarbons. *J. Phys. Chem. A* **105**, 9396–9409 (2001).
47. Ostadhossein, A. et al. ReaxFF reactive force-field study of molybdenum disulfide (MoS_2). *J. Phys. Chem. Lett.* **8**, 631–640 (2017).
48. Froyen, S. & Harrison, W. A. Elementary prediction of linear combination of atomic orbitals matrix elements. *Phys. Rev. B* **20**, 2420–2422 (1979).

Data availability

The data that support the plots within this paper and other findings of this study are available from the corresponding authors upon reasonable request.

Acknowledgements

N.J.B. and P.J.S. acknowledge support from the National Science Foundation through award NSF-1838403. P.J.S. thanks S. Strauf for stimulating and enlightening discussions. J.W.K. acknowledges support from the National Science Foundation through awards NSF-1437450 and NSF-1363093. The preparation and characterization of the nanobubbles in flux-grown low-defect-density WSe_2 were partially supported as part of Programmable Quantum Materials, an Energy Frontier Research Center funded by the US Department of Energy, Office of Science, Basic Energy Sciences (BES), through award DE-SC0019443. C.C., M.F. and F.J. acknowledge financial support from the German Research Foundation (RTG 2247 'Quantum Mechanical Materials Modelling - QM^3') as well as resources for computational time at the HLRN (Hannover/Berlin). E.Y. acknowledges partial support through a US Department of Energy, Office of Science Graduate Student Research (SCGSR) award. K.W. and T.T. acknowledge support from the Elemental Strategy Initiative conducted by MEXT, Japan and CREST (JPMJCR15F3), JST.

Author contributions

P.J.S., N.J.B. and T.P.D. conceived the nano-optical study. Experimental measurements were conducted by T.P.D., E.Y., N.J.B. and A.K. Samples for these measurements were prepared by O.A., J.A., E.Y., A.G., D.A.R., A.N.P. and J.C.H. K.W. and T.T. provided critical materials for the preparation of these samples. The experimental data were analysed by T.P.D., N.J.B. and P.J.S. with important contributions from J.W.K. Theoretical calculations were carried out by C.C., M.F. and F.J. All authors contributed to the preparation of the manuscript.

Competing interests

The authors declare no competing interests.

Additional information

Supplementary information is available for this paper at https://doi.org/10.1038/s41565-020-0730-5.

Correspondence and requests for materials should be addressed to F.J., N.J.B. or P.J.S.